ELSEVIER

Hydrodynamics of a particle impact on a wall

Mark C. Thompson [a,*], Kerry Hourigan [a], Alex Cheung [a], Thomas Leweke [b]

[a] *Fluids Laboratory for Aeronautical and Industrial Research (FLAIR), Department of Mechanical Engineering,*
P.O. Box 31, Monash University, Vic. 3800, Australia
[b] *Institut de Recherche sur les Phénomènes Hors Equilibre (IRPHE), CNRS/Universités Aix-Marseille,*
F-13884 Marseille, France

Abstract

The problem of a particle impacting on a wall, a common phenomenon in particle-laden flows in the minerals and process industries, is investigated computationally using a spectral-element method with the grid adjusting to the movement of the particle towards the wall. Remeshing is required at regular intervals to avoid problems associated with mesh distortion and the constantly reducing maximum time-step associated with integration of the non-linear convective terms of the Navier–Stokes equations. Accurate interpolation between meshes is achieved using the same high-order interpolation employed by the spectral-element flow solver. This approach allows the full flow evolution to be followed from the initial approach, through impact and afterwards as the flow relaxes. The method is applied to the generic two-dimensional and three-dimensional bluff body geometries, the circular cylinder and the sphere. The principal case reported here is that of a particle colliding normally with a wall and sticking. For the circular cylinder, non-normal collisions are also considered. The impacts are studied for moderate Reynolds numbers up to approximately 1200. A cylindrical body impacting on a wall produces two vortices from its wake that convect away from the cylinder along the wall before stalling while lifting induced wall vorticity into the main flow. The situation for a sphere impact is similar, except in this case a vortex ring is formed from the wake vorticity. Again, secondary vorticity from the wall and particle plays a role. At higher Reynolds number, the secondary vorticity tends to form a semi-annular structure encircling the primary vortex core. At even higher Reynolds numbers, the secondary annular structure fragments into semi-discrete structures, which again encircle and orbit the primary core. Vorticity fields and passive tracer particles are used to characterize the interaction of the vortical structures. The evolution of the pressure and viscous drag coefficients during a collision are provided for a typical sphere impact. For a Reynolds number greater than approximately 1000 for a sphere and 400 for a cylinder, the primary vortex core produced by the impacting body undergoes a short-wavelength instability in the azimuthal/spanwise direction. Experimental visualisation using dye carried out in water is presented to validate the predictions.
© 2006 Elsevier Inc. All rights reserved.

Keywords: Vortex dynamics; Particle–wall interactions; Moving grids; Vortex rings

---

* Corresponding author. Tel.: +61 3 9905 9645; fax: +61 3 9905 9639.
  E-mail addresses: mark.thompson@eng.monash.edu.au (M.C. Thompson), kerry.hourigan@eng.monash.edu.au (K. Hourigan).

1. Introduction

Many processes in the minerals and process industries involve the transport and processing of particle-laden fluids. Particle impacts on walls are a source of heat transfer augmentation as well as erosive wear and deposition [1]. Surprisingly, very little visualisation of the fluid mechanics due to the impact of particles on surfaces has been undertaken. The recent article by Eames and Dalziel [2] shows that when a rigid body collides with a surface, a layer of dust on the surface can be resuspended due to the effects of two different mechanisms. The first is ballistic in nature. The collision breaks cohesive bonds between the dust particles and, if the kinetic energy is sufficiently large, this can lead to the ballistic ejection of particles from the wall. For dust ejection by sand particles, experiments by Rice et al. [3], and Shao et al. [4] related the mass ejection rate to the collision rate and the energy loss per collision. The second mechanism leading to dust ejection is hydrodynamic, which is the focus of this article. At particle Reynolds numbers in excess of approximately 100, diffusion is insufficient to prevent the wake of the rigid body overtaking it on impact. The resultant vortex structure(s), originating from the separated flow behind the body, can cause significant dust resuspension. The resuspension occurs after a significant time delay as the wake vorticity advects from behind the body to the wall; this provides a spectacular effect in experimental visualisations. Eames and Dalziel [2] examined the behaviour experimentally in some detail as the Reynolds number was varied between 300 and 3500. They also provided analysis primarily directed towards resuspension characteristics of different dust types and layer thicknesses rather than the fluid dynamics, of primary concern in this paper.

Note that particle impacts with walls also have importance for other areas such as fouling, and the enhancement of heat transfer due to the convection of fluid towards and away from the surface through the action of the wake structures. In addition, the associated momentum transport may significantly affect the bulk flow of multi-phase fluids.

In this paper the numerical method is described and applied to the fluid dynamics associated with normal impacts of generic two- and three-dimensional bodies. The predictions are compared with experimental dye visualisations, which highlight the vortical structures and the induced flow separation at the wall.

2. Methodology

2.1. Numerical method

The numerical approach is based on the spectral-element method e.g., [5]. The particular formulation employed here is based on a *nodal* representation and hence it is effectively a high-order Galerkin finite-element approach. The domain is subdivided coarsely into a set of discrete macro-elements (*h*-discretisation). Internally within elements, higher-order Lagrangian polynomial interpolation is used to approximate solution variables (*p*-discretisation). The node points correspond to Gauss–Legendre–Lobatto quadrature points, which produces considerable efficiency gains in the evaluation of the integrals formed by applying the weighted residual method to the Navier–Stokes equations, and leads to a diagonal mass matrix. The spatial discretisation is based on quadrilateral elements although other possibilities exist which maintain the spectral convergence properties of the method. Of course, a key advantage of *hp*-type methods is that the domain can often be discretised once-only with a sub-optimal macro-element mesh and then an accurate converged solution can be obtained by increasing the order of intra-element polynomial interpolation at runtime until convergence is achieved. Since mesh construction is often time-consuming and user-intensive, this strategy can be of considerable benefit.

The problem considered requires the solution of the time-dependent incompressible Navier–Stokes equations in a domain with moving geometrical elements. The equations are discretized in time through a traditional three-step splitting approach [6], which treats convection, pressure/continuity and diffusion terms as sequential sub-steps. Second-order time accuracy for the velocity field is achieved by applying first- or second-order pressure boundary conditions. Both axi-symmetric and Cartesian versions of the code have been validated extensively for domains without moving boundaries e.g., [7], [8]. Full details of the method can be found in these references and Karniadakis and Sherwin [5].

The modification required to treat moving boundaries is based on the ALE (Arbitrary Lagrangian–Eulerian) method described in, for example, Warburton and Karniadakis [9]. The Navier–Stokes equations and continuity equation, modified to account for the movement of mesh points, is given by

$$\frac{\partial \mathbf{u}}{\partial t} + (\mathbf{u} - \mathbf{u}_{\mathrm{m}}) \cdot \nabla \mathbf{u} = -\nabla p + v \nabla^2 \mathbf{u},$$

$$\nabla \cdot \mathbf{u} = 0.$$

Here $\mathbf{u}$ is the fluid velocity, $\mathbf{u}_{\mathrm{m}}$ is the velocity of the mesh, $p = P/\rho$ is the kinematic pressure, P is the pressure, ρ is the fluid density and v is the kinematic viscosity. The partial derivatives are relative to the moving mesh. The mesh velocity is constrained to match the velocity at moving or stationary boundaries, but can be freely chosen internally. Preferably it should be chosen to lead to minimal mesh distortion as the flow evolves. For the problem considered here, it is difficult to ensure maintenance of a high-quality mesh during the entire evolution. Remeshing is typically required several times during the approach of the body to the wall to minimise the effects of both excessively skewed elements and the continual reduction in the maximum time-step due to the increasingly strong Courant condition. This is true even though the non-linear step is treated semi-implicitly, as discussed below.

Remeshing can be done efficiently using the same high-order tensor-product Lagrangian interpolation employed by the spectral-element scheme within elements. This involves finding each element in the old mesh containing each node point in the new mesh and using polynomial interpolation based of Newton iteration to transfer the solution from the old to the new mesh. In practice, a series of meshes is constructed with the body at different distances from the wall. The flow is evolved for a predetermined time on the first mesh and then the calculation is halted and the velocity field transferred to the next mesh in the sequence. The flow computation is then restarted with the new mesh. This happens several times as the body approaches the wall. The whole process is automated using batch instructions for the time integrations and interpolations allowing the flow to be evolved from the initial impulsive start, through impact and the eventual decay of the vorticity field post-impact.

Apart from the modification of the standard spectral-element implementation to include the spatially dependent mesh velocity, there are two other important modifications required. Although the splitting method is well-known, the equations are supplied here to assist with the following discussion detailing the changes involved for the moving mesh.

The Navier–Stokes and continuity equations given above are discretised in time by integrating over a time-step as follows

$$\int_{t}^{t+\Delta t} \frac{\partial \mathbf{u}}{\partial t} \, \mathrm{d}t = \mathbf{u}^{(n+1)} - \mathbf{u}^{(n)} = (\mathbf{u}^{(n+1)} - \hat{\hat{\mathbf{u}}}) + (\hat{\hat{\mathbf{u}}} - \hat{\mathbf{u}}) + (\hat{\mathbf{u}} - \mathbf{u}^{(n)})$$

$$= -\int_{t}^{t+\Delta t} (\mathbf{u} - \mathbf{u}_{\mathrm{m}}) \cdot \nabla \mathbf{u} \, \mathrm{d}t - \int_{t}^{t+\Delta t} \nabla p \, \mathrm{d}t + v \int_{t}^{t+\Delta t} \nabla^2 \mathbf{u} \, \mathrm{d}t,$$

where the subscript (n) refers to the time level and we have introduced *intermediate* velocities $\hat{\mathbf{u}}$ and $\hat{\hat{\mathbf{u}}}$. Hence, we can break the integration down into three sub-steps treating advection, pressure/continuity and diffusion, respectively

$$\hat{\mathbf{u}} - \mathbf{u}^{(n)} = -\int_{t}^{t+\Delta t} (\mathbf{u} - \mathbf{u}_{\mathrm{m}}) \cdot \nabla \mathbf{u} \, \mathrm{d}t, \tag{1}$$

$$\hat{\hat{\mathbf{u}}} - \hat{\mathbf{u}} = -\int_{t}^{t+\Delta t} \nabla p \, \mathrm{d}t, \tag{2}$$

$$\mathbf{u}^{(n+1)} - \hat{\hat{\mathbf{u}}} = v \int_{t}^{t+\Delta t} \nabla^2 \mathbf{u} \, \mathrm{d}t. \tag{3}$$

Generally, the righthand side of the advection sub-step is treated using a second- or third-order Adams-Bashforth approximation, e.g., for second-order

$$\hat{\mathbf{u}} - \mathbf{u}^{(n)} = -\Delta t \left(\frac{3}{2} ((\mathbf{u} - \mathbf{u}_{\mathrm{m}}) \cdot \nabla \mathbf{u})^{(n)} - \frac{1}{2} ((\mathbf{u} - \mathbf{u}_{\mathrm{m}}) \cdot \nabla \mathbf{u})^{(n-1)} \right). \tag{4}$$

No explicit boundary conditions are required or applied to this equation.

An equation for the pressure can be obtained by taking the divergence of the pressure sub-step equation and enforcing that $\nabla \cdot \hat{\mathbf{u}} = 0$, which, in turn, ensures that the continuity equation is satisfied at the end of the full timestep provided that the velocity field at the previous step was divergence-free. The pressure equation is then given by

$$\nabla^2 p^{(n+\frac{1}{2})} = \frac{1}{\Delta t} \nabla \cdot \hat{\mathbf{u}} \tag{5}$$

and the intermediate velocity update is then given by

$$\hat{\hat{\mathbf{u}}} = \hat{\mathbf{u}} - \Delta t \nabla p^{(n+\frac{1}{2})}. \tag{6}$$

Again, no velocity boundary conditions are required for this equation. The pressure equation requires boundary conditions, which are obtained by dotting the NS equations with the surface normal. The only term contributing from any boundaries for the cases considered is from the diffusion term. Karniadakis et al. [6] describe a stable treatment of this term. Zeroth-order pressure boundary conditions, $\mathbf{n} \cdot \nabla p = 0$ where $\mathbf{n}$ is the surface normal, lead to a first-order accurate velocity approximation. A first-order boundary condition sets $\mathbf{n} \cdot \nabla p^{(n+1/2)} = v \, \mathbf{n} \cdot \nabla^2 \mathbf{u}^{(n)}$, while the second-order condition is $\mathbf{n} \cdot \nabla p^{(n+1/2)} = v\mathbf{n} \cdot \nabla^2 \mathbf{u}^{(n+1/2)}$. Generally, we use the second-order approximation. With the iterative modification to this time-stepping scheme discussed below, a convenient approximation for $\mathbf{u}^{(n+1/2)}$ is $(1/2)(\mathbf{u}_i^{(n+1)} + \mathbf{u}^{(n)})$, where $\mathbf{u}_i^{(n+1)}$ is the current iterative estimate at the next timestep. In practice, using the second-order pressure condition tends to reduce the maximum timestep slightly. Note that for stability reasons it is necessary to use the alternate form of the diffusion term

$$v\nabla^2 \mathbf{u} = v(\nabla(\nabla \cdot \mathbf{u}) - \nabla \times \nabla \times \mathbf{u}).$$

The diffusion sub-step is generally approximated by the second-order Crank–Nicolson method (or the θ variation, see Canuto et al. [10]) giving the following Helmholtz equation

$$\left(1 - \frac{1}{2}v\Delta t\nabla^2\right)(\mathbf{u}^{(n+1)} - \mathbf{u}^{(n)}) = (\hat{\hat{\mathbf{u}}} + \mathbf{u}^{(n)}). \tag{7}$$

The spectral-element method involves the application of the Galerkin weighted residual method to each of the sub-step equations. The shape and weighting functions are Lagrangian interpolating polynomials using element nodal points corresponding to Gauss–Legendre–Lobatto quadrature points in the transformed elements. This leads to sparse matrix equations for the sub-steps associated with pressure and diffusion. For two-dimensional problems on fixed meshes, the matrices are inverted directly using sparse Gaussian elimination or decomposed into LU (upper and lower) triangular matrix form. Hence, the sub-steps reduce to matrix–vector multiplies with fixed matrices. For the case here, the mesh points move from timestep to timestep, which means that the matrices associated with the pressure and viscous sub-steps are a function of time. Hence, it is necessary to solve new matrix equations at each timestep. This adds some overhead to the computation, since this is a relative expensive computational component. The expense increases with the order of the interpolating polynomials used with elements. Generally, it is better to use a lower polynomial order (say 5th or 6th) and increase the number of elements. However, the increased cost of computing the LU decompositions of the sparse matrices at each step is somewhat offset by using an iterative method for the non-linear step. The first iteration uses the explicit Adams-Bashforth form given above but subsequent iterations use

$$\hat{\mathbf{u}}_{i+1} - \mathbf{u}^{(n)} = -\Delta t\left(\frac{1}{2}((\mathbf{u}_i - \mathbf{u}_{\mathrm{m}}) \cdot \nabla \mathbf{u}_i)^{(n+1)} + \frac{1}{2}((\mathbf{u} - \mathbf{u}_{\mathrm{m}}) \cdot \nabla \mathbf{u})^{(n)}\right), \tag{8}$$

where i is the iteration index, so that $\mathbf{u}_i^{(n+1)}$ is the current estimate of $\mathbf{u}$ at the end of a full timestep. Iteration continues until the solution converges. Generally, only two or three iterations are required. For this problem it was found that the maximum timestep could generally be set at about 5–10 times the Courant timestep of the standard splitting approach.

A convenient way to treat non-normal impacts is to only compress the mesh in the normal direction to the wall and handle the tangential velocity component by solving the Navier–Stokes equations in a frame moving uniformly tangentially to the wall. A schematic of the problem geometry and parameters is shown in Fig. 1, showing the physical frame and preferred computational frame. This can be done for both Cartesian and axisymmetric coordinate systems, although at this stage we have only obtained results for the Cartesian code.
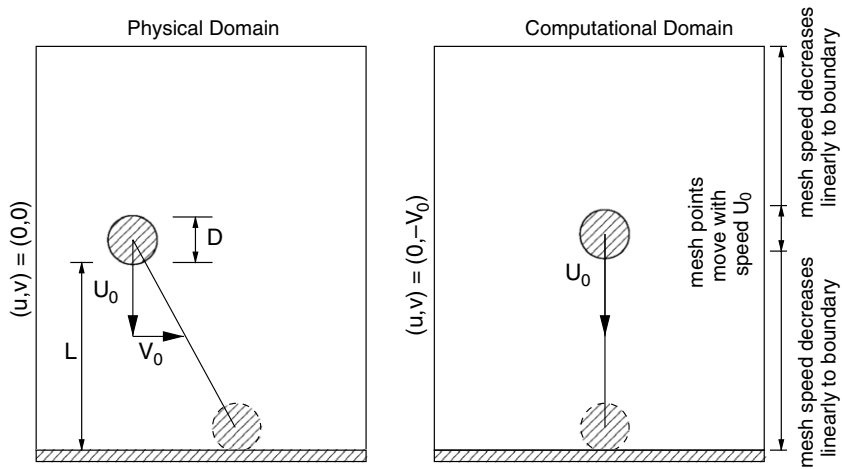
Fig. 1. Schematic of the geometry, problem parameters and boundary conditions.

2.2. Meshing

As described above, several remeshing steps were required as the body approached the wall. Typically, the cylinder or sphere was initially placed at a starting distance of $L = 5D$ from the wall. In agreement with experiments of Eames and Dalziel [2], we find that for starting distances much greater than this, the wake often loses symmetry before impact. A sequence of meshes for modelling normal impact is shown in Fig. 2. Only macro-elements are shown; the mesh is internally subdivided with $N \times N$ nodal points. Typically N is between 5 and 9 depending on the Reynolds number. Only the mesh in the vicinity of the body is shown. All meshes used extend $50D$ upstream and $25D$ in the cross-stream direction, leading to small blockage ratios. For a starting distance of $5D$ it was sufficient to interpolate between meshes twice as shown in the figure.

Care was taken to ensure that remeshing does not introduce significant errors. As a typical example of the size of the effect, for the highest cylinder collision example presented here, $Re = 400$, with $N = 6$, interpolation from the rightmost mesh on the second line in Fig. 2 to the mesh above and back again introduces a *maximum*
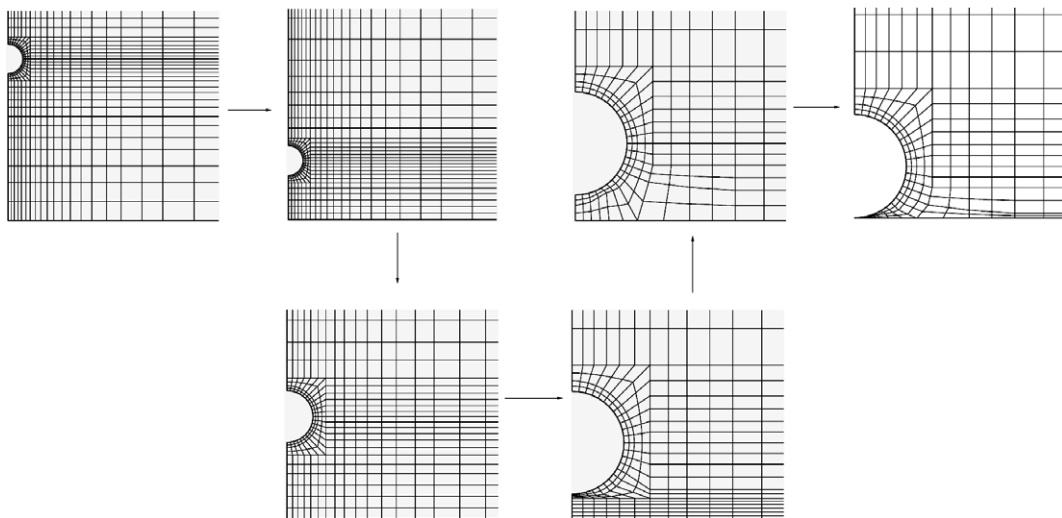

Fig. 2. Sequence of meshes used for the impact studies. Only macro-elements near the body are shown. The horizontal arrow shows mesh evolution with time. The vertical arrows indicate interpolation from one mesh to another.
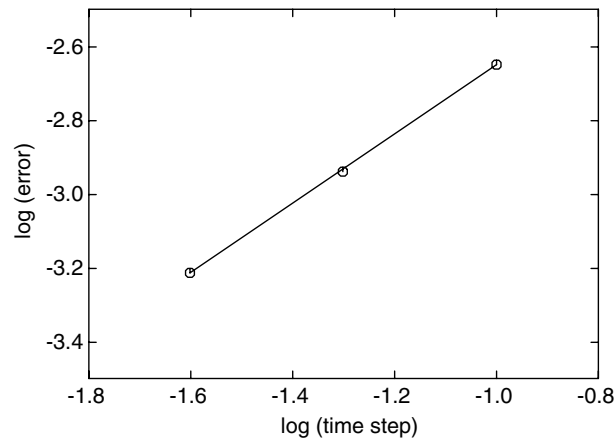
Fig. 3. Log–log plot of error versus timestep for zeroth-order pressure boundary conditions. The slope is unity in line with expectations. The true solution was estimated from using second-order pressure boundary conditions and $\Delta\tau = 0.01$. Even with $\Delta\tau = 0.1$, the wake velocity was accurate to five significant figures.

change in the velocity components of 0.2%. In addition, the drag force varies smoothly across the remeshing step.

2.3. Temporal accuracy

For a stationary mesh, the method is formally second-order accurate provided at least first-order boundary conditions are applied to the Poisson equation for the pressure. Verification of temporal convergence for the current case was shown as follows. The flow for $Re = 100$ and $N = 6$ was initially integrated from an impulsive start for a non-dimensional time of $\tau = tD/U_0 = 1$. This was long enough for a recirculating wake to begin to develop. The polynomial order was sufficiently high to fully resolve the flow for this Reynolds number. The flow was then restarted and integrated for a further 0.5 time units using different timesteps and pressure boundary conditions. At the end of this period, the velocity along the centreline in the wake at $0.25D$ from the rear of the cylinder was recorded. Fig. 3 shows how the error in the velocity varies with timestep for the *zeroth-order* pressure boundary condition. Clearly, the convergence is linear as expected. Using either first- or second-order pressure boundary conditions give five significant figure accuracy even for the largest time-steps used ($\Delta t = 0.1$). Generally, a timestep of 0.005 or less was used for most of the calculations presented in this paper.

2.4. Experimental techniques

Experiments of sphere impacts with a wall were carried out in a $60 \times 50 \times 50$ cm^3 glass tank filled with water. A metal ball 19.02 mm in diameter was attached to a fine twisted nylon thread. The thread passed over a pulley and was wound on a threaded reel driven by a computer-controlled stepper motor. This mechanism allowed the sphere to be lowered through the water at a specified speed, thereby allowing specification of the Reynolds number. Fluorescein dye and light from an Argon ion laser were used to visualise the wake vortical structures and the formation and advection of the vortex ring structures as the wake threaded over the sphere on impact.

3. Results

3.1. Normal collision of a circular cylinder

A series of simulations were completed for a circular cylinder striking a wall normally. This can be considered as effectively a two-dimensional particle. For these computations, the initial starting distance was chosen

to be $L/D = 5$. Recall that Eames and Dalziel [2] found that, for a spherical particle, at this distance the wake remained axi-symmetric and steady prior to impact. We also found a similar restriction in our experiments.

Simulations were run for $Re = 100$, 200 and 400. Fig. 4 shows snapshots of the vorticity field at a sequence of times post-collision. Since it was assumed the wake remains symmetrical at this starting distance only half the domain was simulated with a symmetry boundary condition imposed. The wake overtakes the body after impact and eventually forms into a vortex tube with an almost radially symmetric distribution at long times. As the wake vorticity passes the cylinder, vorticity of opposite sign is generated at the cylinder surface, which also sheds from the cylinder and is convected away. In addition, the vorticity originating from the wake also causes opposite-signed vorticity to be generated at the solid surface below. These two sources of clockwise vorticity encase the stronger anticlockwise vortex tube. The evolution shows a strong effect of Reynolds number. For $Re = 100$, viscous diffusion acts quickly to dissipate the structures, so that at long times, only the remnants of the vortex tube remain. For $Re = 200$, the tube remains partially encased by a still strong annulus of clockwise vorticity. Finally, at $Re = 400$, the secondary annular vortical structure fragments, in much the same way that occurs for a vortex ring striking a wall. The stability of the evolving vortical structures will be considered later.

3.2. Oblique collision of a circular cylinder

Fig. 5 shows the evolution of the vorticity field for different impact angles, θ, measured from the normal. For these three simulations $Re = 100$ based on the normal velocity and distance, and $L/D = 5$ as before. For
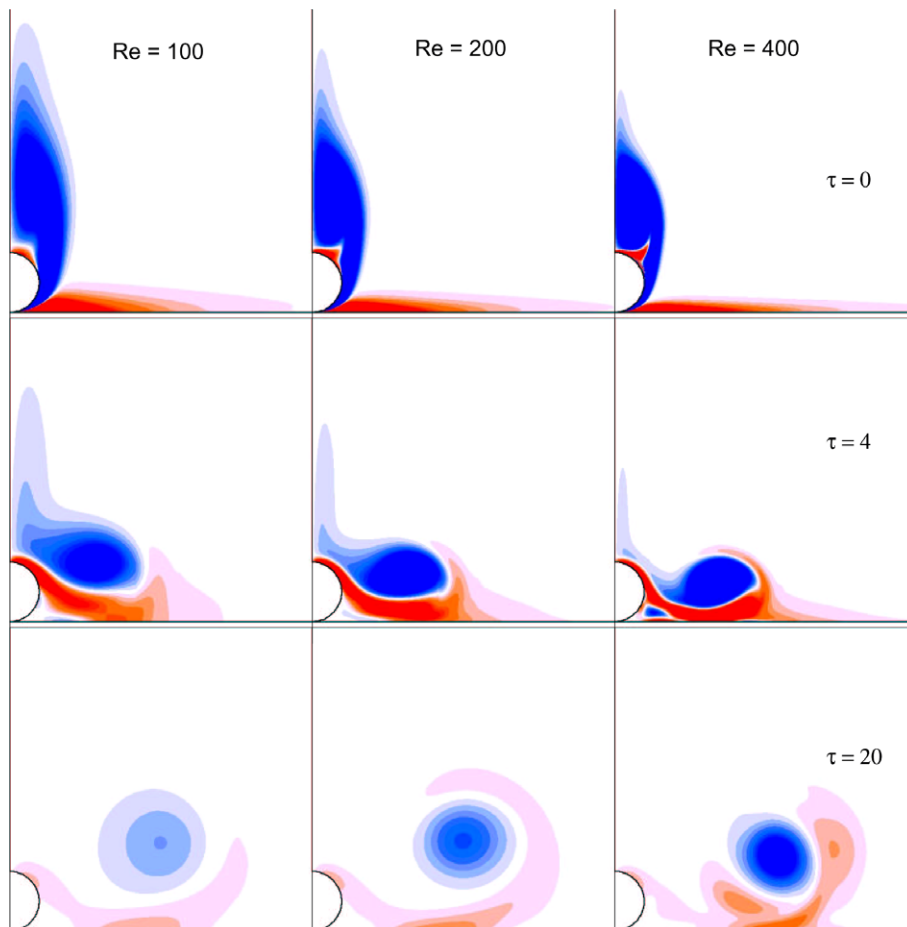

Fig. 4. Vorticity contours showing the vorticity dynamics after the normal impact of a circular cylinder with a wall. Coloured contours levels are the same for all plots allowing the relative effects of diffusion to be gauged.
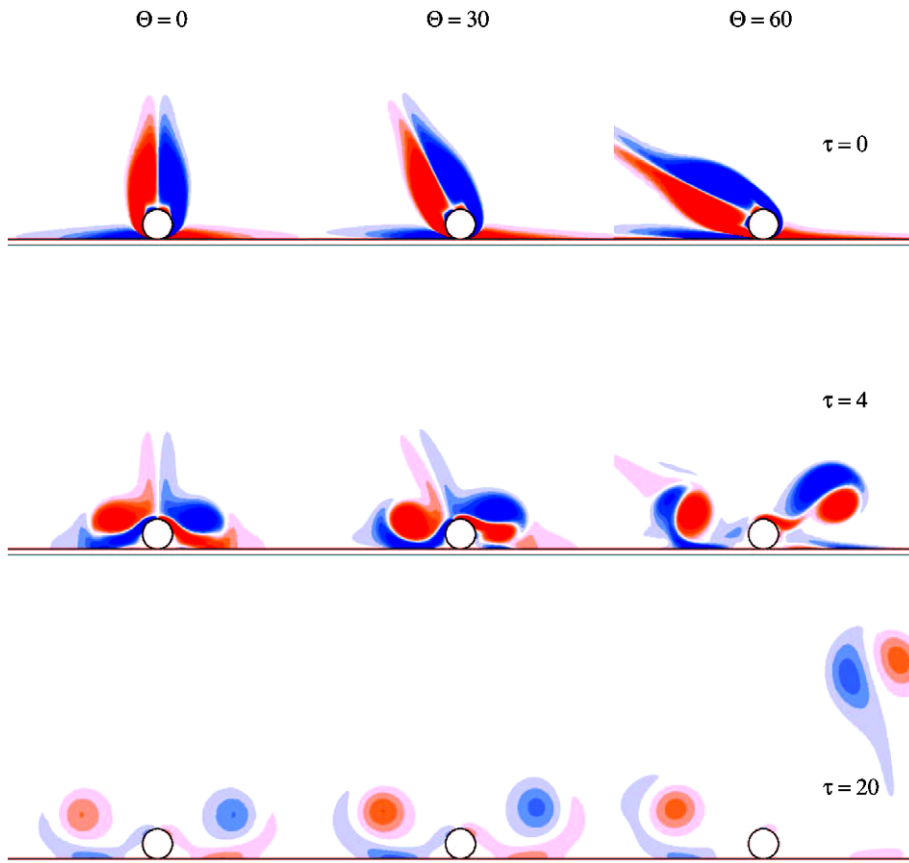
Fig. 5. Dynamics of the vorticity field for non-normal impacts. The Reynolds number is 100.

an impact angle of 30°, the long term vorticity evolution is not very much different from that for a normal impact. The field becomes more symmetrical at long times. At $\theta = 60°$, however, the initial asymmetry is strongly maintained. The vorticity structure on the far side of the impact point consists of the wake vorticity, as before, together with considerable opposite-signed vorticity shed from the cylinder as the primary vorticity passes. These two sources combine together into a vortex pair, consisting of vortices of similar strength. As a consequence, the pair moves along a circle of large radius allowing the pair to advect almost vertically from the wall.

3.3. Sphere impacts

3.3.1. Comparison with experiments

Fig. 6 shows a sequence of images comparing experimental dye visualisations with numerical predictions of the vorticity field for a sphere striking a wall normally at $Re = 500$ and $L/D = 5$. The times correspond to $\tau = 1.5, 4, 8, 16$. The primary vortex ring has reached within 10% of its final radial position by the final time. More detailed results for sphere impacts over a range of Reynolds numbers can be found in Thompson et al. [11].

3.3.2. Mixing of fluid due to impact

A plot of the positions of passive tracer particles for $\tau = 20$ is given in Fig. 7, for a normal sphere impact at $Re = 400$ and $L = 5D$. The particles were initially placed on a regular grid. Their positions were then evolved from the time that the sphere began to move towards the wall until the primary vortex ring had almost reached
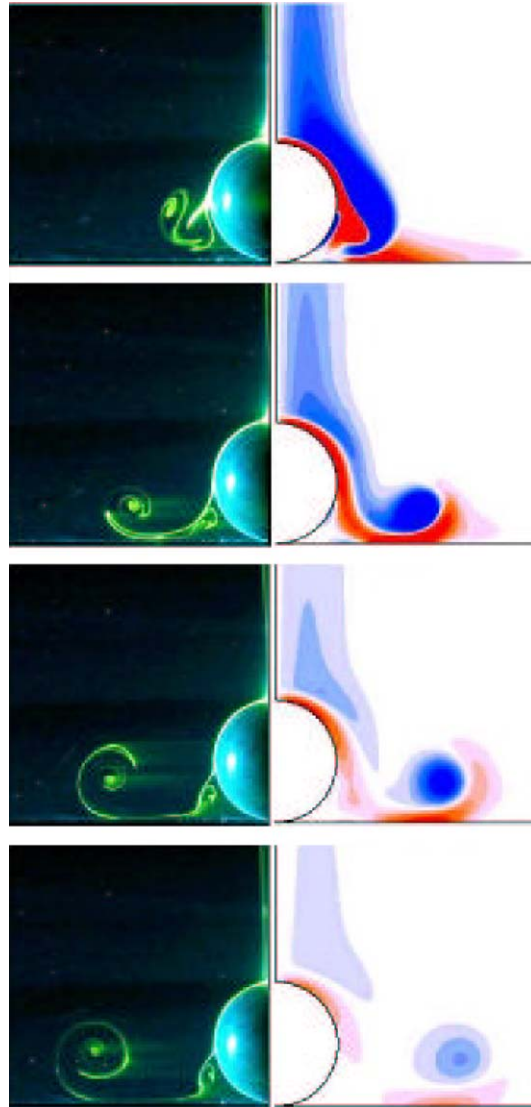
Fig. 6. Comparison of experimental results and numerical predictions for a sphere impact at $Re = 500$ and $L/D = 5$. Lefthand side shows images obtained from dye placed on the sphere. Righthand images are the corresponding numerical vorticity contours.

its final position. The particle positions were integrated in time using the second-order Adams-Bashforth scheme, with spectral-element interpolation used to evaluate the velocities. The particles form a spiral pattern inside the vortex ring similar to the experimental dye visualisations of the previous figure. The total distance travelled by each particle was also recorded during the evolution. Fig. 8 shows a coloured contour plot of the total distance moved (left) and the difference between the final and starting position (right) a function of starting position. As expected the maximum movement occurs for particles close to the initial position of the sphere. There is also a strong effect from the vortex ring system after impact. One interesting question is how much fluid movement is caused by the movement of the sphere? This can be estimated by summing the distance moved for each volume element associated with a particle. The ratio of the volume-weighted distance moved by the fluid relative to the sphere is approximately 7.0. If only the displacement from the original position is considered, then this reduces to approximately 5.0. Either way, moving the sphere through the fluid results in considerable fluid rearrangement.
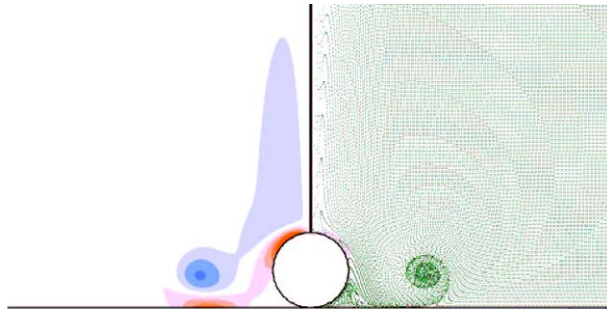
Fig. 7. The position of initially regularly spaced tracer particles at $\tau = 20$ after the impact of a sphere with a wall. The lefthand image shows the vorticity pattern at this time. $Re = 400$ and $L/D = 5$.
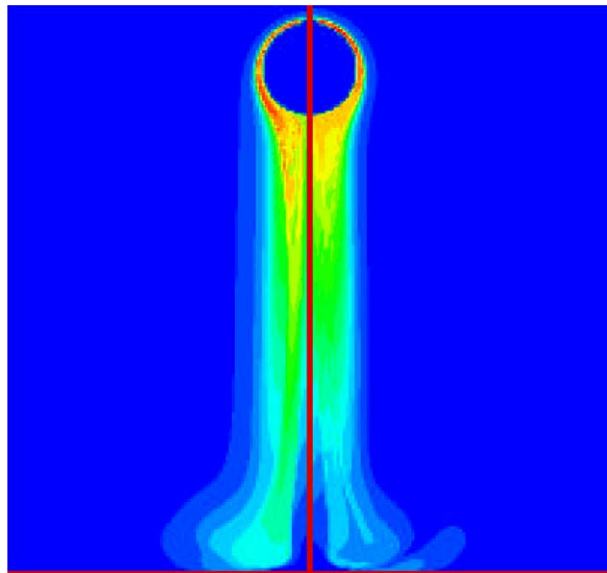

Fig. 8. Coloured contour plot showing the integrated distance (left) and difference between the initial and final positions (right) of tracer particles as a function of initial position. $Re = 400$ and $L/D = 5$.

3.3.3. Spheres at terminal velocity striking a wall

An interesting case not previously examined is that of a sphere falling under gravity so it reaches its terminal velocity and the flow field is fully developed prior to impact. At present only axisymmetric cases are considered. Since a sphere wake remains axisymmetric until $Re = 212$ e.g., Thompson et al. [7], we consider the $Re = 200$ case. At this stage we are not considering the deceleration of the sphere caused by increased fluid forces when the sphere gets close to the wall.

Fig. 9 shows a plot of the pressure (C_p) and viscous (C_v) force coefficients before and after impact. Far from the wall, $C_p = 0.417$ and $C_v = 0.364$, giving a total drag coefficient of 0.78 in good agreement with the experimental result of Roos and Willmarth [12]. The force coefficients remain relatively constant until the sphere gets within about half a diameter from the wall. During the final stages prior to collision, both the viscous and pressure forces increase substantially as the fluid near the wall is squeezed out from the gap between the sphere and wall. After the sphere decelerates to zero velocity impulsively at impact, the force coefficients reverse sign. The viscous force continues to push the sphere towards the wall, as the wake continues to pass over the surface of the sphere. The pressure force changes sign again after impact so that the force is directed away from the wall. However, post-impact the dominant force contribution is from viscous drag. This is not surprising as during this period the effective Reynolds number gradually reduces to zero.
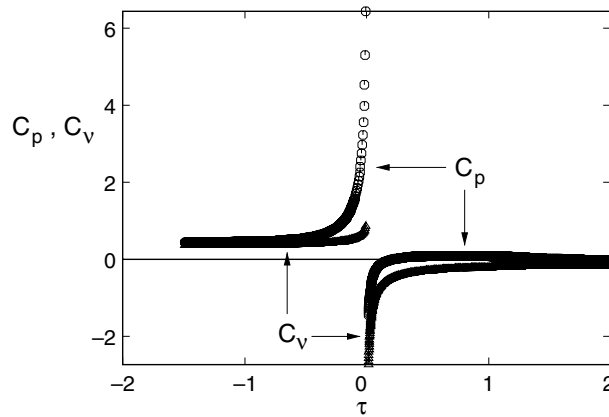
Fig. 9. Pressure (circles) and viscous (triangles) force coefficient histories during the normal impact of a sphere with a wall. $Re = 200$ and $L/D \to \infty$.
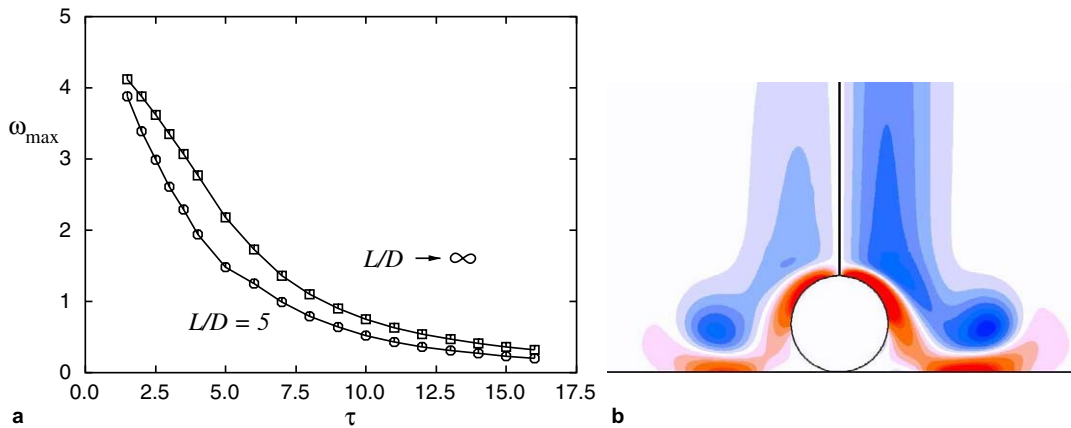

Fig. 10. (a) Vorticity evolution at the centre of the vortex ring formed after the impact of a sphere with a wall at $Re = 200$. Results for two starting distances are given. (b) Vorticity field at $\tau = 10$ for $L/D = 5$ (left) and $L/D \to \infty$ (right).

In Fig. 10(a) the evolution of the vorticity at the centre of the main vortex ring is shown for $Re = 200$, both for $L/D = 5$ and for when the wake is essentially in equilibrium prior to impact, i.e. $L/D \to \infty$, as discussed above. It takes some time for a distinct vortex ring to develop, hence only results for $\tau > 1.5$ are given. Initially, there is little difference in strength between the two vortex structures, despite the significant difference in pre-collision wake strength and length. This is probably due to the similar vorticity density in both wakes near the rear of the sphere. However, at longer times the wake for $L/D \to \infty$ can continue to supply circulation at a higher rate, and for longer, and hence the decay of the central vorticity is slower in this case. Fig. 10(b) shows the vorticity distribution for both cases at $\tau = 10$ using the same contour levels. This highlights the relative similarity of the vortical structures despite the difference strengths.

3.4. Three-dimensional instabilities

Previous experiments by Eames and Dalziel [2], which focused on dust ejection, showed that above a Reynolds number of about 1000, the vortex ring system formed during sphere impact developed a three-dimensional instability. Our own experiments and simulations also show this to occur. Fig. 11 shows an experimental dye visualisation together with a computer-generated isosurface visualisation of (perturbation) radial vorticity. In both cases $Re = 1200$ and $L/D = 5$. The instability wavelength is of the order of $1D$ or less. This is
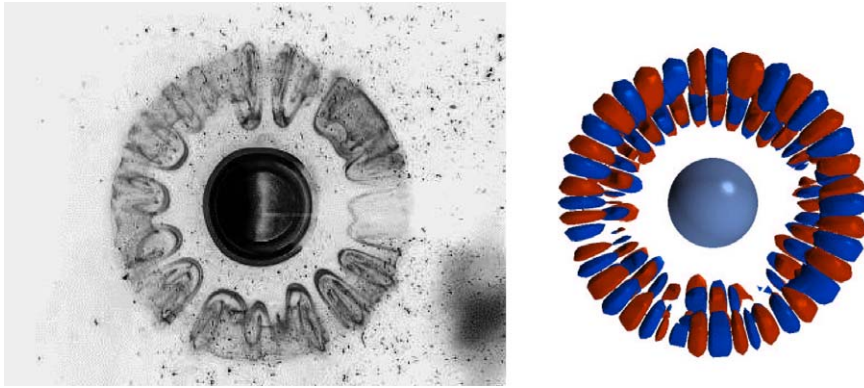
Fig. 11. Left: Dye visualisation of the development of the instability for a sphere impact. (Note the negative image is shown.) Right: positive and negative isosurfaces of radial vorticity obtained from the seeded three-dimensional computation at a similar time. For both cases $Re = 1200$ and $L/D = 5$.

much shorter than the dominant wavelength of the instability examined by Swearingen et al. [13] for vortex rings interacting with a solid surface. In that case, the instability can be associated with the straining of weaker secondary vortex rings by the primary vortex ring as it orbits. For typical vortex ring wall impacts studied by Orlandi and Verzicco [14] and Swearingen et al. [13], the fragmenting of the secondary vorticity shed from the wall as it orbits is similar to the situation shown in Fig. 4 at $\tau = 20$ for $Re = 400$, for the two-dimensional particle impact. These secondary vortex rings develop a longer wavelength instability under the strain field of the primary ring. This mechanism probably contributes at longer times for sphere impacts if the secondary vorticity surrounding the primary core fragments, and may dominate for higher Reynolds number collisions. The shorter wavelength instability has been examined in some detail in Thompson et al. [11] for sphere collisions, with the conclusion that it is likely related to a centrifugal instability due to the opposite-signed secondary vorticity surrounding the primary ring.

It appears that this short-wavelength instability will also occur in the two-dimensional analogue, i.e. a circular cylinder striking a wall. This possibility was examined numerically by transferring the velocity field for the $Re = 400$ impact, as shown in Fig. 4, to a three-dimensional spectral spectral-element code and evolving
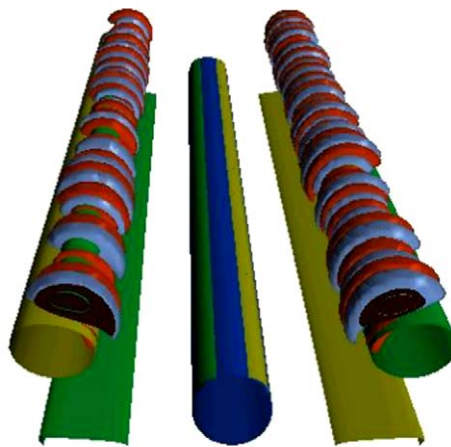

Fig. 12. Isosurface plot showing the development of the three-dimensional instability outside the primary vortex core after a cylinder collision with a wall. Isosurfaces of the spanwise vorticity shows the location of the main vortex tubes. Axial vorticity isosurfaces show the short wavelength instability developing near the location of the orbiting secondary vortex tube. In addition, the position of the cylinder is shown and the wall vorticity beneath the primary cores can be seen. Here, $Re = 400$, $L/D = 5$ and $\tau = 11$.

the flow further. To encourage the growth of three-dimensionality, the velocity field was seeded with a low-level white-noise perturbation. The spanwise domain size was chosen to be 16*D* and 128 Fourier planes were used.

The flow was integrated until $\tau = 11$. Fig. 12 shows a visualization of the perturbation axial vorticity field at the final time. This vorticity component was zero initially. Iso-surfaces of spanwise vorticity are also shown to indicate the position of the primary vortex tube and encircling secondary tubes. Clearly, the perturbation is maximum in the vicinity of one of the secondary vortex tubes, similar to the situation found for the sphere impact. The dominant wavelength is considerably less than 1*D*, also in agreement with sphere impact studies. The secondary vortex tube has very little kinking at this stage, hence the straining mechanism proposed by Swearingen et al. [13] is yet to have much effect. However, measurements of the overall amplification of the axial perturbation vorticity over this time interval indicates it is comparable to that observed for the sphere impact case at $Re = 1200$, for a comparable interval. Since experiments [15], [2] show that the three-dimensional instability can be observed for $Re \gtrsim 1000$ for sphere impacts with typical background noise levels, it seems reasonable to conclude that a similar instability may be observed at lower Reynolds numbers of $Re = 400$ or less for cylinder impacts.

4. Conclusions

A series of numerical predictions of the impact (and sticking) of both a circular cylinder and a sphere have been undertaken, with validating experiments. The spectral-element method incorporating a deforming mesh based on the ALE (Arbitrary Lagrangian–Eulerian) method has successfully predicted the formation and evolution of vortex tubes (for the cylinder) or rings (for the sphere), validated by dye visualisation experiments. The spreading vortex ring or tubes cause significant fluid mixing near the wall leading to dust resuspension. It is expected that the heat transfer properties would be also significantly modified by the influence of the vortical structures. In particular, collisions at large impact angles may lead to strong vortex pairs developing, which may advect and transport fluid to considerable distances from the impact zone.

As the Reynolds number is increased above approximately 1000 for a sphere or 400 for a cylinder, three-dimensionality appears in the spreading vortex ring/tube. The instability has a wavelength of less than the particle diameter and most of the amplification occurs during the initial 10 time units after impact. At later times, and possibly at at higher Reynolds numbers, the vortex straining instability proposed by Swearingen et al. [13] probably also plays a strong role.

Although the present studies are fundamental in nature and idealised, they do indicate that the hydrodynamics associated with particle impacts on walls can be significant, and can be an important factor in heat and mass transport, and particle resuspension, in lightly loaded flows relevant to mineral and process industries.

References

[1] G.G. Joseph, R. Zenit, M.L. Hunt, A.M. Rosenwinkel, Particle–wall collisions in a viscous fluid, J. Fluid Mech. 433 (2001) 329–346.
[2] I. Eames, S.B. Dalziel, Dust resuspension by the flow around an impacting sphere, J. Fluid Mech. 403 (2000) 305–328.
[3] M.A. Rice, B.B. Willetts, I.K. McEwan, Wind erosion of crusted solid sediments, Earth Surf. Proc. Land. 21 (1996) 279–293.
[4] Y. Shao, M.R. Raupach, P.A. Findlater, Effect of saltation bombardment on the entrainment of dust by the wind, J. Geophys. Res. 98 (1993) 12719–12726.
[5] G.Em. Karniadakis, S.J. Sherwin, Spectral/HP Element Methods for CFD, first ed., Oxford University Press, England, 1999.
[6] G.E. Karniadakis, M. Israeli, S.A. Orszag, High-order splitting methods of the incompressible Navier–Stokes equations, J. Comput. Phys. 97 (1991) 414–443.
[7] M.C. Thompson, T. Leweke, M. Provansal, Kinematics and dynamics of sphere wake transition, J. Fluids Struct. 15 (2001) 575–585.

[8] G.S. Sheard, M.C. Thompson, K. Hourigan, From spheres to circular cylinders: non-axisymmetric transition in the flow past rings, J. Fluid Mech. 506 (2004) 45–78.

[9] T.C. Warburton, G.Em. Karniadakis, Spectral simulations of flow past a cylinder close to a free surface, in: ASME Fluid Engineering Division Summer Meeting 1997, pages FEDSM97—3389 (CDROM), 1997.

[10] C. Canuto, M. Hussaini, A. Quarteroni, T. Zang, Spectral Methods in Fluid Dynamics, second ed., Springer Verlag, Berlin and New York, 1990.

[11] M.C. Thompson, T. Leweke, K. Hourigan, Vortex dynamics associated with a sphere colliding normally with a surface, J. Fluid Mech., under review.

[12] F.W. Roos, W.W. Willmarth, Some experimental results on sphere and disk drag, AIAA J. 9 (2) (1971) 285–291.

[13] J.D. Crouch, J.D. Swearingen, R.A. Handler, Dynamics and stability of a vortex ring impacting a solid boundary, J. Fluid Mech. 297 (1995) 1–28.

[14] P. Orlandi, R. Verzicco, Vortex rings impinging on walls: axisymmetric and three-dimensional simulations, J. Fluid Mech. 256 (1993) 615–646.

[15] T. Leweke, M.C. Thompson, K. Hourigan, Vortex dynamics associated with the collision of a sphere with a wall, Phys. Fluids (Lett.) 16 (9) (2004) 74–77.